ACS APPLIED MATERIALS & INTERFACES

www.acsami.org

Research Article

Interlayer Registry Dictates Interfacial 2D Material Ferroelectricity

Wei Cao, Oded Hod,* and Michael Urbakh

Cite This: *ACS Appl. Mater. Interfaces* 2022, 14, 57492−57499

Read Online

ACCESS | Metrics & More | Article Recommendations | Supporting Information

ABSTRACT: We discover that the complex ferroelectric response of layered materials toward interlayer sliding is fully dictated by the interlayer lattice registry. Importantly, the entire sliding polarization landscape of two-dimensional (2D) layered material interfaces is fully described via a simple and intuitive geometric measure, termed the polarization registry index (PRI), that quantifies the degree of interlayer commensurability. Beyond the understanding of the fundamental origin of 2D ferroelectricity, the developed tool also provides highly efficient characterization and rationalization of existing experimental and computational evidence of 2D interfacial ferroelectricity, as well as the prediction of emergent controllable polarization in new noncentrosymmetric layered systems.

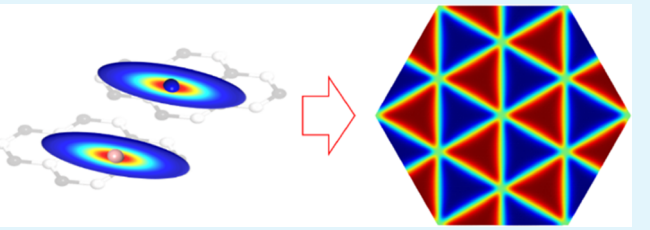

KEYWORDS: *registry index, slidetronics, polarization, vdW, twist, h-BN, TMD*

1. INTRODUCTION

Ferroelectricity is a material property where a switchable spontaneous electric polarization emerges due to broken centrosymmetry of the crystal structure. On its 100th anniversary, the field entered uncharted territories of two-dimensional (2D) ferroelectric van der Waals materials.[1−3] One of the first realizations was demonstrated using hexagonal boron nitride (h-BN) bilayer structures, stacked in their parallel configuration to break centrosymmetry.[4−6] Introducing a small twist angle between neighboring h-BN layers leads to surface reconstruction, which is characterized by a triangular superlattice of adjacent AB and BA stacked regions of opposite electric polarization. The domain walls separating these commensurate regions can be shifted via external electric fields, thus allowing control over the local polarization of the system—a phenomenon termed "slidetronics".[4] Going beyond atomically thin h-BN-based systems, ferroelectricity has been demonstrated also in members of the transition-metal dichalcogenide (TMD) family, characterized by an intricate sublayer structure.[7−12]

Polarization in layered material interfaces is intimately related to their interlayer stacking mode, which dictates the global symmetry, relative atomic positions, and interlayer charge transfer. Therefore, ferroelectricity in these materials can be achieved via interplane displacements. This calls for developing quantitative relations between interlayer commensurability and the emergent interfacial polarization.[13−16] In this paper, we harness the power of the registry index (RI)[17−24]—a quantitative measure of interlayer lattice commensurability—to reveal direct correlation between interlattice registry and interfacial electric polarization in layered materials. The developed tools enable the efficient and accurate prediction and characterization of electric polarization patterns in complex layered material structures while circumventing heavy-duty quantum mechanical electronic structure calculations.

2. RESULTS AND DISCUSSION

2.1. Polarization Registry Index for Bilayer h-BN. To demonstrate the global polarization registry index (GPRI) approach, we first consider bilayer h-BN, stacked in its parallel interlayer orientation, which lacks inversion symmetry.[4−6] The degree of atomic registry is characterized by representing each atomic center with a two-dimensional lateral Gaussian function and evaluating the laterally projected overlap, s_{in}, between Gaussian pairs associated with atoms i and n, residing in adjacent layers

$$s_{in} = \frac{2\pi\sigma_{t_i}^{t_n^2}\sigma_{t_n}^{t_i^2}}{\sigma_{t_i}^{t_n^2} + \sigma_{t_n}^{t_i^2}} e^{-(d_{in}^2/2(\sigma_{t_i}^{t_n^2} + \sigma_{t_n}^{t_i^2}))} \quad (1)$$

Here, d_{in} is the lateral distance between the two atoms and $\sigma_{t_i}^{t_n}$ is the Gaussian width of atoms of type t_i in one layer interfacing an atom of type t_n in its adjacent layer.[23] With this, the GPRI expression for h-BN may be defined as follows:

$$\mathrm{GPRI}^{\text{h-BN}} = \frac{S_{\mathrm{BN}} - S_{\mathrm{NB}}}{S_{\mathrm{BN}}^{\max} - S_{\mathrm{NB}}^{\max}} \quad (2)$$

Received: November 13, 2022
Accepted: November 30, 2022
Published: December 15, 2022

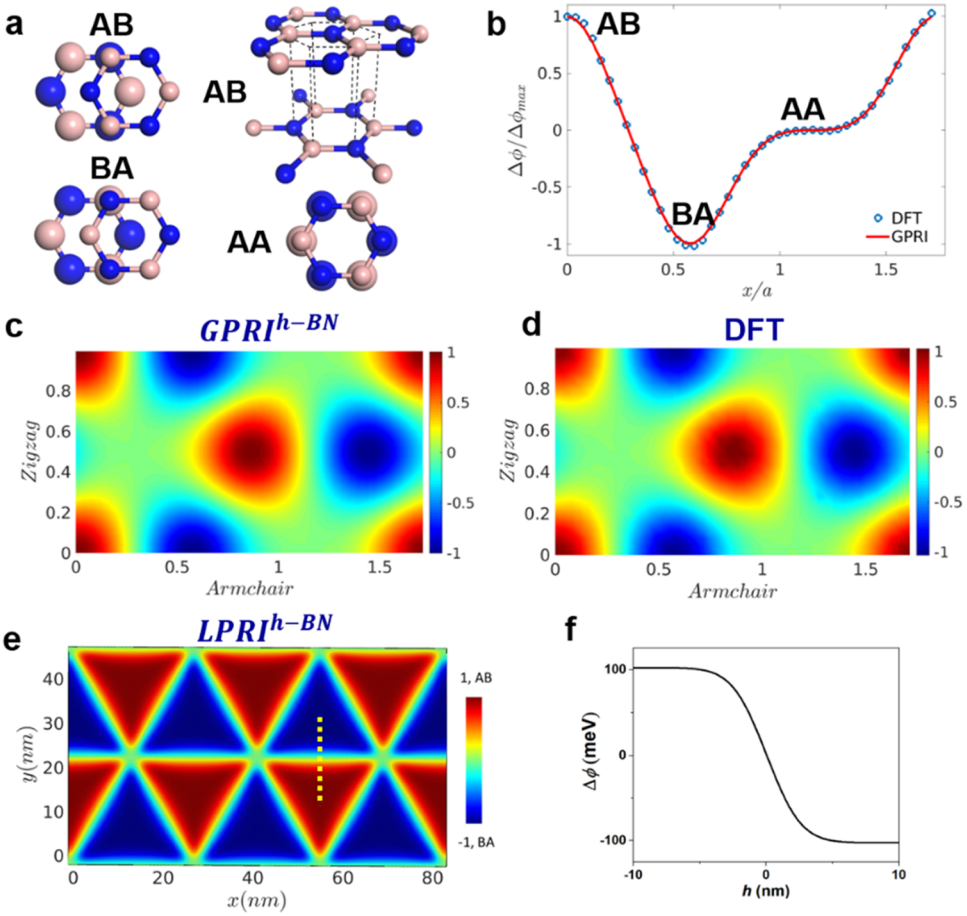

Figure 1. (a) High-symmetry stacking configurations (AB, BA, and AA) of parallelly stacked bilayer h-BN. Blue and pink spheres represent N and B atoms, respectively. In the top views, the upper (lower) layer atoms are represented by small (large) spheres. For the AB stacking mode, a side view is also provided. (b) Polarization profiles calculated using DFT (blue open circles) and the $GPRI^{h\text{-}BN}$ (full red line) for vertically relaxed shifts along the armchair direction. The DFT curve is normalized by the potential drop calculated for the initial AB stacked bilayer ($\Delta\phi_{max}$ (h-BN) = 103 meV). Unnormalized polarization profiles are presented in SI Section 1.3. The *x*-axis is normalized by the intralayer lattice constant of h-BN (a = 2.51 Å). (c) Two-dimensional $GPRI^{h\text{-}BN}$ map obtained using the same parameters extracted from fitting against one-dimensional reference data (see panel (b)). Here, the axes are normalized by the intralayer lattice constant of h-BN. (d) Two-dimensional DFT potential drop landscape, normalized by its maximal value ($\Delta\phi_{max}$(h-BN)). (e) Local polarization registry index ($LPRI^{h\text{-}BN}$) map calculated for a 0.5° twisted AB stacked h-BN bilayer following geometry relaxation using a dedicated classical interlayer potential (see SI Section 1.5). (f) Line cut through the $LPRI^{h\text{-}BN}$ map across a domain wall (see yellow dashed line in panel (e)).

where $S_{T^{top}T^{bot}} = \sum_{i\in T^{top}} \sum_{n\in T^{bot}} s_{in}$ is the sum of pairwise projected Gaussian overlaps, s_{in}, between all atoms of type T^{top} (=B or N) in the top layer with all atoms of type T^{bot}(=B or N) in the bottom layer, and $S^{max}_{T^{top}T^{bot}}$ is the corresponding overlap sum obtained at the AB stacking mode that exhibits the maximal polarization. Note that this expression considers only the dipolar contributions of partially charged B−N and N−B atomic pairs on adjacent layers to the overall polarization, while neglecting minor contributions (typically below 1%) that may arise from homonuclear atomic pairs.

The Gaussian widths appearing in eq 1 are determined against reference density functional theory (DFT) calculations of the out-of-plane polarization, evaluated from the electrostatic potential drop across the h-BN bilayer, at a set of stacking modes along an interlayer sliding path in the armchair direction (see Section 4 and Supporting Information SI Section 1.1 for details). To this end, an AB stacked h-BN bilayer model (see Figure 1a) is first constructed from two individual preoptimized layers (see coordinates at the end of the SI). Then the top layer is shifted with respect to the lower one along the armchair direction, and the vertical coordinates of all atoms are allowed to relax, while fixing their lateral positions. The $GPRI^{h\text{-}BN}$ effective radii are tuned against the corresponding DFT polarization profile for the same set of interlayer configurations. More details regarding the fitting procedure can be found in SI Section 1.2.

A comparison of the DFT (blue open circles) and $GPRI^{h\text{-}BN}$ (full red line) profiles for h-BN interlayer lateral shifts is shown in Figure 1b. To assure that the $GPRI^{h\text{-}BN}$ at the nonpolar AA stacking mode vanishes, we choose $\sigma^N_B = \sigma^B_N$. Excellent agreement between the GPRI profile and the reference data is obtained for effective radii of $\sigma^N_B = \sigma^B_N = 0.22b$, where $b = a/\sqrt{3}$, and a = 2.51 Å is the intralayer lattice constant. The remarkable agreement between the $GPRI^{h\text{-}BN}$ curves and the reference polarization profiles signifies the central role of the lattice registry in dictating the ferroelectric properties of layered materials. We note that the differences between the DFT rigid shift polarization profile and the vertically flexible one are very small (see Figure S1 in SI Section 1.2). Hence, even given unrelaxed geometries, the PRI can provide valuable insights.

https://doi.org/10.1021/acsami.2c20411
ACS Appl. Mater. Interfaces 2022, 14, 57492−57499

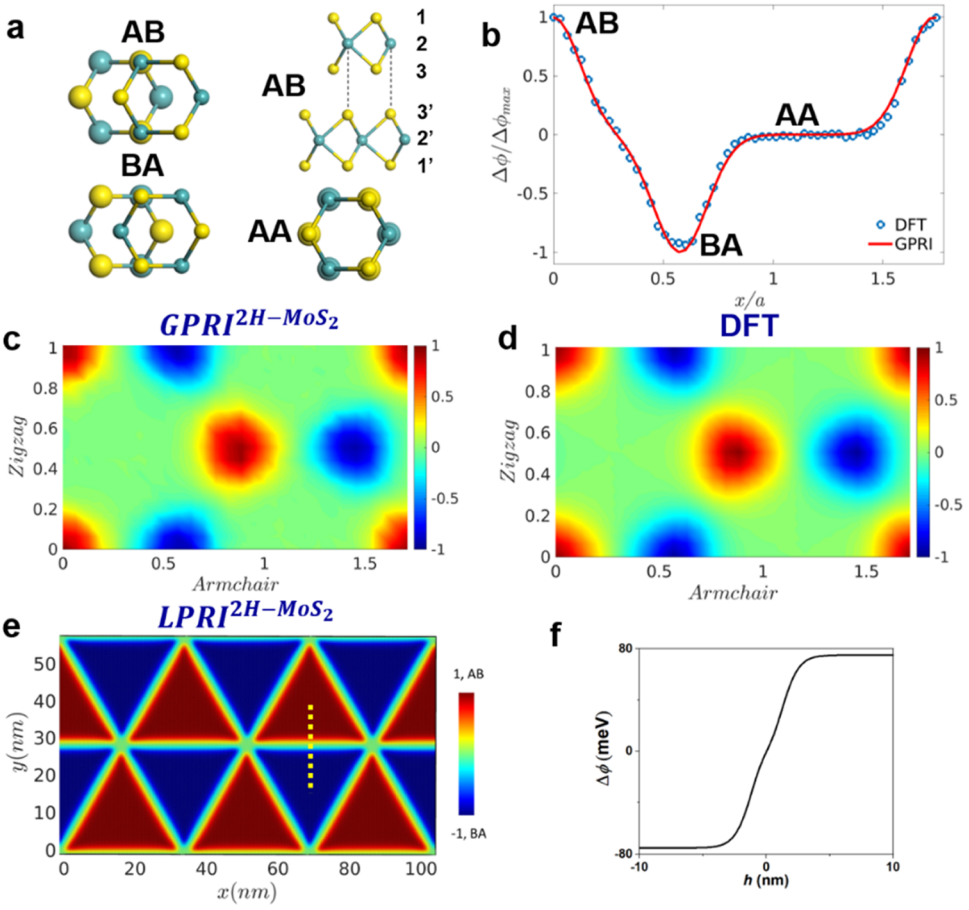

Figure 2. (a) High-symmetry stacking configurations (AB, BA, and AA) of parallelly stacked bilayer MoS_2. Blue and yellow spheres represent Mo and S atoms, respectively. In the top views, the upper (lower) layer atoms are represented by small (large) spheres. For the AB stacking mode, a side view is also provided, where the sublayers are marked by numbers. (b) Polarization profiles calculated using DFT (blue open circles) and the $GPRI^{2H\text{-}MoS_2}$ (full red line) for vertically relaxed shifts along the armchair direction. The DFT curve is normalized by the potential drop calculated for the initial AB stacked bilayer ($\Delta\phi_{max}$ (MoS_2) = 76 meV). Unnormalized polarization profiles are presented in SI Section 2.4. The x-axis is normalized by the intralayer lattice constant of MoS_2 (a = 3.156 Å). (c) Two-dimensional $GPRI^{2H\text{-}MoS_2}$ map obtained using the same parameters extracted from fitting against one-dimensional reference data (see panel (b)). Here, the axes are normalized by the intralayer lattice constant of MoS_2. (d) Two-dimensional normalized DFT potential drop landscape, normalized by its maximal value ($\Delta\phi_{max}$ (MoS_2) = 76 meV). (e) $LPRI^{2H\text{-}MoS_2}$ map constructed for a 0.5° twisted AB stacked MoS_2 bilayer following geometry relaxation using a dedicated classical interlayer potential (see SI Section 2.6). (f) Line cut through the $LPRI^{2H\text{-}MoS_2}$ map across a domain wall (see yellow dashed line in (e)).

To demonstrate the predictive power of the developed geometric measure, we extend the $GPRI^{h\text{-}BN}$ sliding curve into a two-dimensional sliding map (see Figure 1c), using the same parameters fit against the one-dimensional DFT polarization profile. Here, the $GPRI^{h\text{-}BN}$ landscape is in excellent agreement with the reference DFT data (see Figure 1d). The unnormalized DFT data and the difference between $GPRI^{h\text{-}BN}$ landscape and the normalized DFT map are presented in SI Section 1.4.

The GPRI approach can be extended to describe spatially resolved polarization maps at a given stacking configuration. To this end, we define the local polarization registry index ($LPRI^{h\text{-}BN}(i)$) at atomic position i in the top layer by applying eq 2 for atom i and each of its three nearest neighbors, p (within the same layer), and averaging over the results obtained for the three i–p pairs. In practice, this is done by calculating the $GPRI^{h\text{-}BN}$ while ignoring all atoms in the top layer apart from atom i and one of its three neighbors, p_1, then repeating this calculation for the i–p_2 and i–p_3 pairs, and setting the $LPRI^{h\text{-}BN}(i)$ as the average of the three results.

To demonstrate the capabilities of the LPRI, we applied it to a 0.5° twisted AB stacked h-BN bilayer, relaxed using a dedicated interlayer potential (ILP)[25] (see SI Section 1.5 for further details regarding the geometry relaxation). Figure 1e presents the obtained $LPRI^{h\text{-}BN}$ polarization map for all top layer atoms, which nicely reproduces the triangular surface potential landscape measured for this material using Kelvin probe atomic force microscopy.[4] Notably, the domain wall width, estimated from a line cut (see Figure 1f) through the $LPRI^{h\text{-}BN}$ map (see the dashed yellow line in Figure 1e) to be ~10 nm, is also consistent with experimental observations.[4]

2.2. Polarization Registry Index for Homogeneous 2H-TMD Bilayers. The same approach can be used to link polarization and interlayer registry in other layered material interfaces exhibiting ferroelectric characteristics, such as parallelly stacked 2H-TMD bilayers. Unlike atomically flat h-BN, TMDs possess a sublayer structure, where each layer consists of a metal sublayer bridging two chalcogenide sublayers. In the context of polarization evaluation, we find it sufficient to include in the PRI expressions only the projected Gaussian overlaps between atoms residing in the internal four

https://doi.org/10.1021/acsami.2c20411
ACS Appl. Mater. Interfaces 2022, 14, 57492−57499

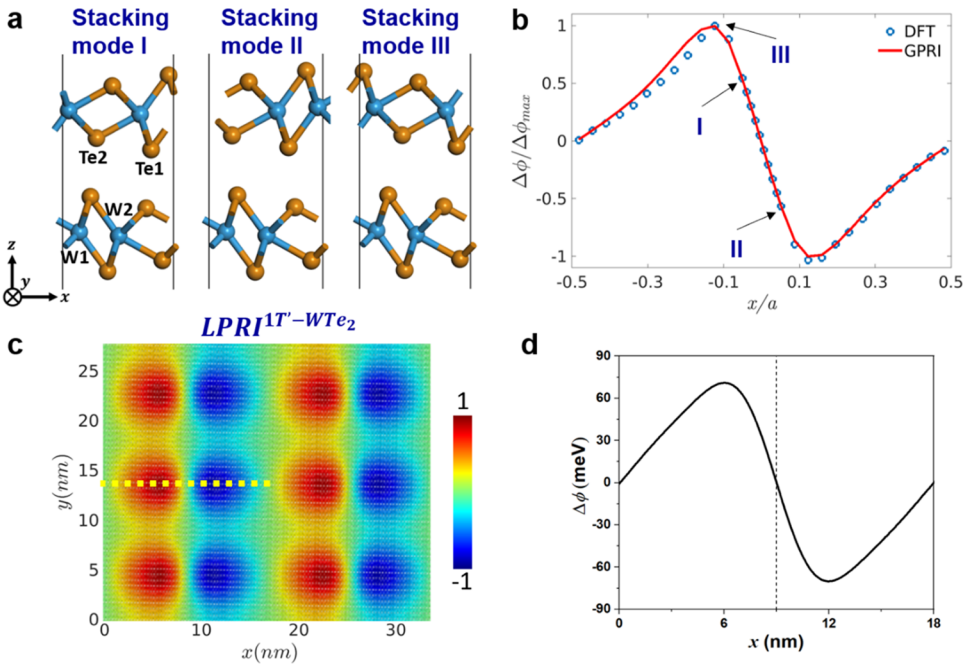

Figure 3. (a) High-symmetry stacking modes of bilayer 1T′ WTe_2 along the x direction. The lowest-energy stacking modes I and II have the same energy and opposite out-of-plane polarization. Stacking mode III exhibits the largest polarization along the x-direction. Atomic labels as per eq 3 are presented for stacking mode I. (b) x Direction polarization profile calculated using DFT (blue open circles) and the $GPRI^{1T'\text{-}WTe_2}$ (full red line). The DFT curve is normalized by the potential drop calculated for stacking mode III ($\Delta\phi_{max}(1T'\text{-}WTe_2)$ = 64 meV). The x-axis values are normalized by the intralayer lattice constant of 1T′ WTe_2 along the x direction (a = 6.26 Å). (c) An $LPRI^{1T'\text{-}WTe_2}$ map for a 2° rigidly twisted 1T′ WTe_2 bilayer. $LPRI^{1T'\text{-}WTe_2} = \pm 1$ represent stacking mode III and its mirror image in the x−y plane. (d) $LPRI^{1T'\text{-}WTe_2}$ profile along the dashed yellow line appearing in (c). The $LPRI^{1T'\text{-}WTe_2}$ results are scaled by $\Delta\phi_{max}(1T'\text{-}WTe_2)$ to obtain an estimate of the potential drop across the domain wall separating regions of stacking modes I and II, whose position is marked by the vertical black dashed line.

sublayers of a bilayer stack (numbered as 2, 2′, 3, 3′ in Figure 2a), neglecting all overlaps with Gaussians associated with atoms residing in the external chalcogen sublayers (numbered as 1 and 1′ in Figure 2a). As such, only three nearest neighbors of each atom in each TMD layer are considered, similar to the case of h-BN. Therefore, we can use the same expression of eq 2 replacing B with M (signifying the metal atom) and N with X (the corresponding chalcogen).

The performance of the PRI for homogeneous 2H-TMD bilayers is demonstrated for the case of parallelly stacked bilayer MoS_2 in Figure 2. The effective radii obtained by fitting against DFT polarization profiles (see Section 4 and SI Section 2.1 for details) obtained for vertically flexible shifts (see Figure 2b) with the same level of theory as that used above for h-BN are: $\sigma_{Mo}^{S} = \sigma_{S}^{Mo} = 0.15b$, where $b = a/\sqrt{3}$ and a = 3.156 Å is the lattice constant. Excellent agreement is found between the $GPRI^{2H\text{-}MoS_2}$ and the reference DFT data, indicative of the intimate relation between vertical polarization and interlattice registry in noncentrosymmetric TMD interfaces. Similar to the case of h-BN discussed above, the 2D $GPRI^{2H\text{-}MoS_2}$ landscape (see Figure 2c), calculated using the same parameter set, captures well the corresponding DFT polarization map (see Figure 2d). The unnormalized DFT data and the difference between the $GPRI^{2H\text{-}MoS_2}$ landscape and the normalized DFT data are presented in SI Section 2.5. Furthermore, the 2D $LPRI^{2H\text{-}MoS_2}$ map (see Figure 2e), calculated as in the case of h-BN for a relaxed 0.5° twisted AB stacked MoS_2 bilayer (see SI Section 2.6),[26] reproduces well the polar domain pattern found using piezoelectric[9] and Kelvin probe atomic force microscopy[10] experiments. Figure 2f presents the $LPRI^{2H\text{-}MoS_2}$ potential drop profile across a domain wall along the dashed yellow line appearing in Figure 2e. The domain wall width of ∼4 nm, estimated from this profile, is consistent with experimental observations.[10] PRI parameterizations for other members of the layered TMD family, including $MoSe_2$, WS_2, and WSe_2, and the corresponding analyses are presented in SI Section 2.2.

2.3. Polarization Registry Index for 1T′-WTe_2 Bilayer.

The correlation between lattice registry and electric polarization extends beyond the 2H-hexagonal structure of TMD materials discussed above. To demonstrate this, we consider the 1T′ phase of a WTe_2 bilayer, where switching of polarization was predicted to occur when the bilayer is shifted between stacking modes I and II of Figure 3a.[27] Here, we find it sufficient to consider only contributions of projected Gaussian overlaps between W and Te atoms residing in the internal sublayers of the two adjacent WTe_2 layers (see Figure 3a) for the description of the polarization profile. Due to the distorted structure of the 1T′ phase, however, there are two inequivalent W and Te positions within the unit cell (excluding the external Te sublayers, see Figure 3a), which we mark as $W_{1,2}$ and $Te_{1,2}$, respectively. With this, the $GPRI^{1T'\text{-}WTe_2}$ is defined as follows

$$GPRI^{1T'\text{-}WTe_2} = \frac{S_{WTe} - S_{TeW}}{S_{WTe}^{max} - S_{TeW}^{max}} \tag{3}$$

Here, $S_{T^{top}T^{bot}} = \sum_{r=1}^{2}\sum_{s=1}^{2}\sum_{i\in T_r^{top}}\sum_{n\in T_s^{bot}} s_{in}$, $T_{1(2)}^{top}$ and $T_{1(2)}^{bot}$ = $W_{1(2)}$ *or* $Te_{1(2)}$, and s_{in} is the projected overlap between Gaussians associated with atoms i and n, residing on adjacent

https://doi.org/10.1021/acsami.2c20411
ACS Appl. Mater. Interfaces 2022, 14, 57492−57499

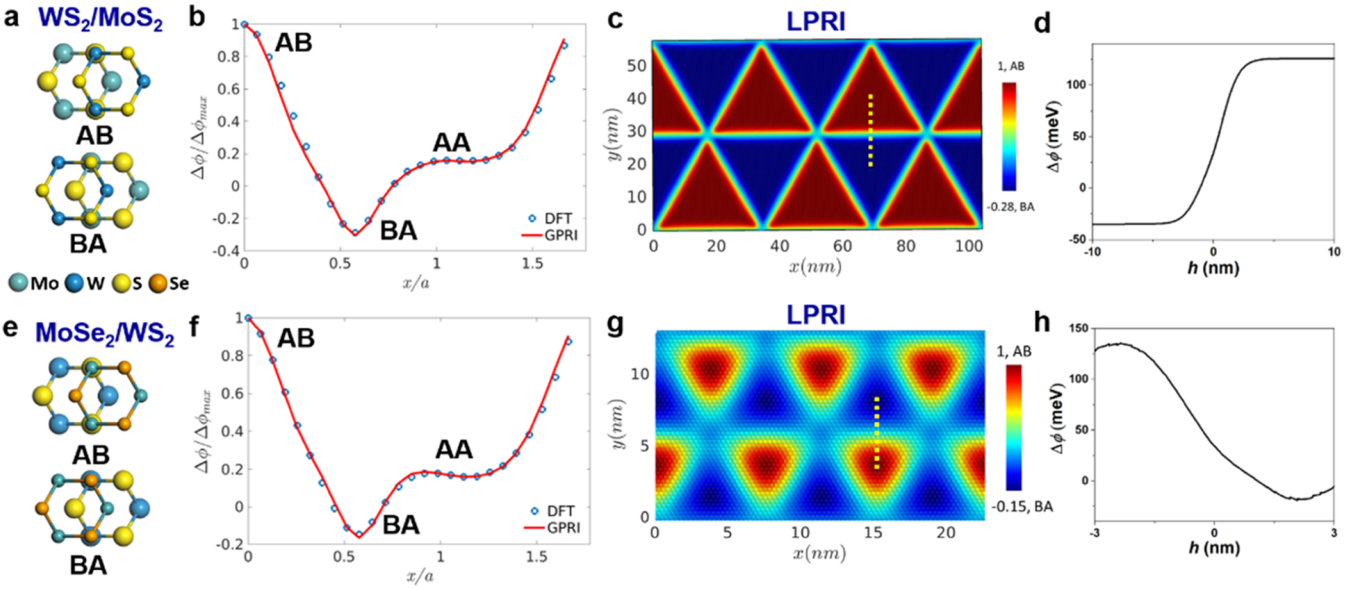

Figure 4. (a) High-symmetry stacking configurations (AB and BA) of parallelly stacked bilayer WS_2/MoS_2. The upper (lower) layer atoms are represented by small (large) spheres. For the heterogeneous interfaces, the lateral lattice vectors of the bilayer are chosen as the average of the corresponding lattice vectors of the relaxed individual layers, which are stretched or compressed accordingly to form the supercell. Since WS_2 and MoS_2 have a negligible lattice mismatch, the lattice constant of a = 3.187 Å for the bilayer is practically the same as that of the individual monolayers. (b) Polarization profile calculated using DFT (open blue circles) and the $GPRI^{WS_2/MoS_2}$ (full red line) along the armchair direction. The DFT curve is normalized by the polarization of the AB stacking mode ($\Delta\phi_{max}$ (WS_2/MoS_2) = 126 meV). (c) $LPRI^{WS_2/MoS_2}$ map calculated for a 0.5° twisted AB stacked WS_2/MoS_2 bilayer following geometry relaxation. (d) Line cut through the $LPRI^{WS_2/MoS_2}$ polarization map across a domain wall (dashed yellow line in (c)) scaled by $\Delta\phi_{max}$ (WS_2/MoS_2). (e–h) Same as (a–d), respectively, for the heterogeneous $MoSe_2/WS_2$ bilayer, having a lattice mismatch of ∼4%. The supercell lattice constant of a = 3.252 Å is taken as the average of the lattice constants of monolayer $MoSe_2$ (a_1 = 3.316 Å) and WS_2 (a_2 = 3.187 Å), obtained using DFT (see SI Section 4.1). The DFT curve in (f) is normalized by the polarization of the AB stacked $MoSe_2/WS_2$ bilayer ($\Delta\phi_{max}$ ($MoSe_2/WS_2$) = 135 meV). The $LPRI^{MoSe_2/WS_2}$ map in (g) is calculated for the unstressed aligned interface following geometry relaxation.

layers, with the appropriate pairwise widths. To account for the different vertical distances between inequivalent W and Te atoms on adjacent layers, we scale the projected overlaps by an exponential function, $f(h_{in}) = \exp[-\alpha(h_{in} - h_{in}^0)]$, that describes the dependence of the polarization on the pairwise vertical interatomic distance, h_{in}, due to variations in the charge transfer, as follows

$$s_{in} = f(h_{in}) \times \frac{2\pi\sigma_{t_i}^{t_n^2}\sigma_{t_n}^{t_i^2}}{\sigma_{t_i}^{t_n^2} + \sigma_{t_n}^{t_i^2}} e^{-(d_{in}^2/2(\sigma_{t_i}^{t_n^2}+\sigma_{t_n}^{t_i^2}))} \quad (4)$$

Here, h_{in}^0 is set to the vertical distance between atoms i and n at stacking mode I, and the exponent α is used as an additional parameter fitted against DFT polarization profile reference data (see Figure 3b, Section 4, and SI Sections 3.1 and 3.2).

Due to the intricate nonhexagonal sublayer lattice structure of WTe_2, vertically flexible shifts were found to yield polarization profiles with unphysical roughness (see SI Section 3.3). Therefore, we resorted to nudged elastic band (NEB) calculations to obtain intermediate configurations between the high-symmetry stacking modes along the sliding path.[27,28] Specifically, we chose the lowest-energy stacking modes I and II (see Figure 3a) as our anchors and stretched the image bands between them along the positive and negative x directions. The resulting polarization profile (open blue circles in Figure 3b) was then used to determine the $GPRI^{1T'\text{-}WTe_2}$ parameters yielding: $\sigma_{W_1}^{Te_1} = \sigma_{Te_1}^{W_1} = 0.01a$, $\sigma_{W_1}^{Te_2} = \sigma_{Te_2}^{W_1} = 0.16a$, $\sigma_{W_2}^{Te_1} = \sigma_{Te_1}^{W_2} = 0.07a$, $\sigma_{W_2}^{Te_2} = \sigma_{Te_2}^{W_2} = 0.18a$, α = 0.77 Å^{-1}, where a = 6.26 Å is the intralayer lattice constant along the x direction. With these parameters, the $GPRI^{1T'\text{-}WTe_2}$ profile (solid red line in Figure 3b) agrees well with the DFT reference data. We note that the Gaussian widths associated with the Te_2–$W_{1(2)}$ pairs are larger than those obtained for the Te_1–$W_{1(2)}$ pairs. This is consistent with the fact that Te_2 atoms possess a larger effective charge than their Te_1 counterparts (see SI Section 3.2). Using the same set of parameters, good agreement is also obtained between the $GPRI^{1T'\text{-}WTe_2}$ and DFT profiles along the y direction (see SI Section 3.2). We therefore find that even for WTe_2—a semimetallic layered material possessing a complex and less symmetric intralayer atomic arrangement—the polarization profile is dictated by interlayer registry.

Similar to the case of h-BN, a local polarization registry index, $LPRI^{1T'\text{-}WTe_2}$, can be defined for 1T′-WTe_2, the only difference being that for any given atom, one should average the $GPRI^{1T'\text{-}WTe_2}$ values of four atomic unit cells corresponding to 10 of its intralayer nearest neighbors, to obtain the $LPRI^{1T'\text{-}WTe_2}$ score (see SI Section 3.4). Figure 3c shows a spatially resolved polarization map of a 2° rigidly twisted mode I stacked 1T′-WTe_2 bilayer, demonstrating adjacent domains of opposite polarization separated by narrow domain walls. The high polarization regions, both positive (red) and negative (blue), correspond to the high-registry (low energy) stacking configurations I and II. Two types of domain walls, with zero polarization (green), also appear. The first, along x = 0 nm (and 18 nm), corresponds to regions of low registry (high stacking energy), whereas the second narrower domain wall, appearing along x = 9 nm (and 27 nm), corresponds to high-registry regions of intermediate stacking energy separating

https://doi.org/10.1021/acsami.2c20411
ACS Appl. Mater. Interfaces 2022, 14, 57492−57499

configurations I and II. We therefore find that while the two domain walls exhibit zero polarization, the nature of their stacking configuration is significantly different. We note that the fact that different stacking modes can provide vanishing polarization is also exemplified in Figure 3b for $x/a = \pm 0.5$ and $x/a = 0$. Figure 3d shows the different potential drops obtained along a line cut crossing the two domain walls separating regions of stacking modes I and II (see the yellow dashed line in Figure 3c), further exemplifying their different nature.

2.4. Polarization Registry Index for Heterogeneous 2H-TMD Bilayers. The PRI approach is not limited to homogeneous noncentrosymmetric interfaces and can be readily applied to describe the polarization in heterogeneous layered contacts. To demonstrate this, we consider the heterogeneous 2H-TMD bilayers of WS_2/MoS_2 and $MoSe_2/WS_2$, for which multiscale modeling has been previously used to describe the moiré ferroelectricity of their twisted structures.[16,29] We denote the general chemical composition of heterogeneous TMD bilayers as M_1X_1/M_2X_2, where in the present case $M_{1/2}$ = Mo or W and $X_{1/2}$ = S or Se. The GPRI for the heterojunction is then defined as follows

$$\mathrm{GPRI}^{\mathrm{M_1X_1/M_2X_2}} = \frac{S_{\mathrm{M_1X_2}} - S_{\mathrm{X_1M_2}} + S_{\mathrm{M_1M_2}} - S_{\mathrm{X_1X_2}}}{S^{\max}_{\mathrm{M_1X_2}} - S^{\max}_{\mathrm{X_1M_2}} + S^{\max}_{\mathrm{M_1M_2}} - S^{\max}_{\mathrm{X_1X_2}}} \quad (5)$$

where, as for the case of homogeneous TMD interfaces, $S_{T^{\mathrm{top}}T^{\mathrm{bot}}} = \sum_{i\in T^{\mathrm{top}}}\sum_{n\in T^{\mathrm{bot}}} s_{in}$, T^{top} = M_1 or X_1, T^{bot} = M_2 or X_2, and s_{in} is given by eq 1.

The DFT polarization profile for the parallelly stacked WS_2/MoS_2 bilayer (see Figure 4a) along the armchair direction is obtained using the NEB method,[28] at the same level of electronic structure theory used in the homogeneous bilayer TMDs calculations (see Section 4 and SI Section 4.1 for further details). Excellent agreement between the reference data (open blue circles) and the $\mathrm{GPRI}^{\mathrm{WS_2/MoS_2}}$ profile (full red line) is obtained (see Figure 4b) using the following parameters: $\sigma^{\mathrm{S}}_{\mathrm{W}} = \sigma^{\mathrm{W}}_{\mathrm{S}} = 0.22b$, $\sigma^{\mathrm{S}}_{\mathrm{Mo}} = \sigma^{\mathrm{Mo}}_{\mathrm{S}} = 0.12b$, $\sigma^{\mathrm{W}}_{\mathrm{Mo}} = \sigma^{\mathrm{W}}_{\mathrm{Mo}} = 0.18b$, $\sigma^{\mathrm{S}}_{\mathrm{S}} = 0.16b$, where $b = a/\sqrt{3}$, and a = 3.187 Å is the lattice constant (taken to be the same for both layers). Notably, the $\mathrm{GPRI}^{\mathrm{WS_2/MoS_2}}$ approach is able to capture the inherent asymmetry between the AB and BA vertical polarizations of the heterogeneous interface. Figure 4c presents an $\mathrm{LPRI}^{\mathrm{WS_2/MoS_2}}$ map for a 0.5° twisted AB stacked WS_2/MoS_2 bilayer, calculated as for the case of homogeneous TMD interfaces. The structure was preoptimized using an appropriately parameterized Kolmogorov–Crespi force field (see SI Section 4.5),[30] yielding an array of triangular domains, separated by narrow domain walls, similar to previous predictions.[29] The $\mathrm{LPRI}^{\mathrm{WS_2/MoS_2}}$ map suggests that adjacent triangular domains exhibit opposite polarization and the domain walls possess a zero polarization line. The $\mathrm{LPRI}^{\mathrm{WS_2/MoS_2}}$ potential drop across the domain walls (dashed yellow line in Figure 4c), scaled by $\Delta\phi_{\max}$ (WS_2/MoS_2) = 126 meV, is presented in Figure 4d.

The heterogeneous $MoSe_2/WS_2$ bilayer has an interlayer lattice mismatch of ~4%. Hence, to perform the NEB DFT calculations (see SI Section 4.1 for details) we constructed a stressed bilayer unit cell with a lattice parameter taken to be the average of the lattice constants of the relaxed individual layers (see Figure 4e). Figure 4f shows excellent agreement between the reference DFT data (open blue circles) and $\mathrm{GPRI}^{\mathrm{MoSe_2/WS_2}}$ profile (full red line) using the following parameters: $\sigma^{\mathrm{Se}}_{\mathrm{W}} = \sigma^{\mathrm{W}}_{\mathrm{Se}} = 0.1b$, $\sigma^{\mathrm{S}}_{\mathrm{Mo}} = \sigma^{\mathrm{Mo}}_{\mathrm{S}} = 0.23b$, $\sigma^{\mathrm{W}}_{\mathrm{Mo}} = \sigma^{\mathrm{W}}_{\mathrm{Mo}} = 0.17b$, $\sigma^{\mathrm{Se}}_{\mathrm{S}} = \sigma^{\mathrm{Se}}_{\mathrm{S}} = 0.19b$, where $b = a/\sqrt{3}$, and a = 3.252 Å is the lattice constant of the stressed supercell. For completeness, the unnormalized polarization profiles are presented in SI Section 4.4. An $\mathrm{LPRI}^{\mathrm{MoSe_2/WS_2}}$ map for the aligned unstressed $MoSe_2/WS_2$ supercell, relaxed using a Kolmogorov–Crespi-type force field[30] (see SI Section 4.5), is presented in Figure 4g. We find that this system exhibits smaller domains of opposite polarization, compared to the marginally twisted WS_2/MoS_2 interface discussed above, with less sharp domain walls (see Figure 4h for a cut along the dashed yellow line in Figure 4g).

Similar results are found for all other bilayer heterojunctions formed between MoS_2, $MoSe_2$, WS_2, and WSe_2 (see SI Section 4.2), demonstrating the generality and transferability of the PRI approach, even to complex interfaces.

3. CONCLUSIONS

The results presented above therefore clearly demonstrate that vertical polarization in noncentrosymmetric layered interfaces is dictated by interfacial registry. This is a highly nontrivial conclusion, considering that the underlying physics involves complex and delicate effects including inter- and intralayer charge transfer and atomic rearrangement. Based on this general understanding, we developed the polarization registry index—a physically intuitive and highly computationally efficient geometric approach to characterize the interfacial polarization in a variety of homogeneous and heterogeneous layered interfaces, including h-BN, as well as hexagonal and nonhexagonal TMDs. With appropriate parameterization, performed only once per interface, the approach agrees well with both DFT reference data of the global polarization of aligned interfaces and recent experimental observations of spatially resolved polarization landscapes in twisted layered interfaces. Notably, even when using rigid material models, the developed PRI provides reliable polarization assessments, let alone in combination with efficient classical force fields that account for geometry relaxation effects, where the approach demonstrates remarkable predictive power. This, in turn, allows us to address polar layered material structures that are beyond the reach of current first-principles computational approaches. For example, in the context of slidetronics,[4] the PRI can be used as an efficient tool to predict and characterize the variation of the polarization map during superlubric interfacial sliding of large lattice mismatch heterojunctions.[31] We note that this predictive power of the PRI approach is not limited to the case of h-BN or TMDs and should be readily extendable to other layered material interfaces.

4. COMPUTATIONAL DETAILS

Reference density functional theory calculations were performed using the plane-wave pseudopotential Quantum Espresso package and the Vienna Ab initio Simulation Package.[32,33] The Perdew–Burke–Ernzerhof generalized gradient exchange–correlation functional approximation was used along with the scalar-relativistic projector augmented wave description of the core electrons.[34] Van der Waals interlayer interactions were evaluated using the Grimme-D3 dispersion correction with Becke–Johnson damping.[35,36] The plane-wave cutoff energy was set to 37–60 Ry (depending on the specific material) with a k-mesh of 12 × 12 × 1 points using the Monkhorst–Pack[37] scheme. A vacuum size of 10 nm along the

https://doi.org/10.1021/acsami.2c20411
ACS Appl. Mater. Interfaces 2022, 14, 57492–57499

normal direction was used to avoid interactions between adjacent bilayer images. To evaluate the vertical polarization of the system, the dipole correction was implemented and the resulting difference between the electrostatic potential values obtained above the top and below the bottom surfaces was calculated. Further details relating to the reference DFT calculations of specific materials are provided in the Supporting Information.

■ ASSOCIATED CONTENT

Supporting Information

The Supporting Information is available free of charge at https://pubs.acs.org/doi/10.1021/acsami.2c20411.

Further details regarding the development of the polarization registry index for bilayer h-BN, homogeneous 2H-TMD bilayers, bilayer 1T′-WTe_2, and heterogeneous 2H-TMD bilayers (PDF)

■ AUTHOR INFORMATION

Corresponding Author

Oded Hod − *Department of Physical Chemistry, School of Chemistry, The Raymond and Beverly Sackler Faculty of Exact Sciences and The Sackler Center for Computational Molecular and Materials Science, Tel Aviv University, Tel Aviv 6997801, Israel;* orcid.org/0000-0003-3790-8613; Email: odedhod@tauex.tau.ac.il

Authors

Wei Cao − *Department of Physical Chemistry, School of Chemistry, The Raymond and Beverly Sackler Faculty of Exact Sciences and The Sackler Center for Computational Molecular and Materials Science, Tel Aviv University, Tel Aviv 6997801, Israel;* orcid.org/0000-0001-5227-7632

Michael Urbakh − *Department of Physical Chemistry, School of Chemistry, The Raymond and Beverly Sackler Faculty of Exact Sciences and The Sackler Center for Computational Molecular and Materials Science, Tel Aviv University, Tel Aviv 6997801, Israel;* orcid.org/0000-0002-3959-5414

Complete contact information is available at: https://pubs.acs.org/10.1021/acsami.2c20411

Notes

The authors declare no competing financial interest.

■ ACKNOWLEDGMENTS

W.C. acknowledges the financial support of the Israel Academy of Sciences and Humanities and the Sackler Center for Computational Molecular and Materials Science at Tel Aviv University. M.U. acknowledges the financial support of the Israel Science Foundation, grant no. 1141/18 and the ISF-NSFC joint grant 3191/19. O.H. is grateful for the generous financial support of the Israel Science Foundation under grant no. 1586/17, the Heineman Chair in Physical Chemistry, Tel Aviv University Center for Nanoscience and Nanotechnology, and the Naomi Foundation for generous financial support via the 2017 Kadar Award.

■ REFERENCES

(1) Tsymbal, E. Y. Two-Dimensional Ferroelectricity by Design. *Science* **2021**, *372*, 1389−1390.

(2) Wu, M.; Li, J. Sliding Ferroelectricity in 2D van der Waals Materials: Related Physics and Future Opportunities. *Proc. Nat. Acad. Sci. U.S.A.* **2021**, *118*, No. e2115703118.

(3) Wu, M. Two-Dimensional Van Der Waals Ferroelectrics: Scientific and Technological Opportunities. *ACS Nano* **2021**, *15*, 9229−9237.

(4) Vizner Stern, M.; Waschitz, Y.; Cao, W.; Nevo, I.; Watanabe, K.; Taniguchi, T.; Sela, E.; Urbakh, M.; Hod, O.; Ben Shalom, M. Interfacial Ferroelectricity by van der Waals Sliding. *Science* **2021**, *372*, 1462−1466.

(5) Yasuda, K.; Wang, X.; Watanabe, K.; Taniguchi, T.; Jarillo-Herrero, P. Stacking-Engineered Ferroelectricity in Bilayer Boron Nitride. *Science* **2021**, *372*, 1458−1462.

(6) Woods, C. R.; Ares, P.; Nevison-Andrews, H.; Holwill, M. J.; Fabregas, R.; Guinea, F.; Geim, A. K.; Novoselov, K. S.; Walet, N. R.; Fumagalli, L. Charge-Polarized Interfacial Superlattices in Marginally Twisted Hexagonal Boron Nitride. *Nat. Commun.* **2021**, *12*, No. 347.

(7) Fei, Z.; Zhao, W.; Palomaki, T. A.; Sun, B.; Miller, M. K.; Zhao, Z.; Yan, J.; Xu, X.; Cobden, D. H. Ferroelectric Switching of a Two-Dimensional Metal. *Nature* **2018**, *560*, 336−339.

(8) de la Barrera, S. C.; Cao, Q.; Gao, Y.; Gao, Y.; Bheemarasetty, V. S.; Yan, J.; Mandrus, D. G.; Zhu, W.; Xiao, D.; Hunt, B. M. Direct Measurement of Ferroelectric Polarization in a Tunable Semimetal. *Nat. Commun.* **2021**, *12*, No. 5298.

(9) Wang, X.; Yasuda, K.; Zhang, Y.; Liu, S.; Watanabe, K.; Taniguchi, T.; Hone, J.; Fu, L.; Jarillo-Herrero, P. Interfacial Ferroelectricity in Rhombohedral-Stacked Bilayer Transition Metal Dichalcogenides. *Nat. Nanotechnol.* **2022**, *17*, 367−371.

(10) Weston, A.; Castanon, E. G.; Enaldiev, V.; Ferreira, F.; Bhattacharjee, S.; Xu, S.; Corte-Leon, H.; Wu, Z.; Clark, N.; Summerfield, A.; Hashimoto, T.; Gao, Y.; Wang, W.; Hamer, M.; Read, H.; Fumagalli, L.; Kretinin, A. V.; Haigh, S. J.; Kazakova, O.; Geim, A. K.; Fal'ko, V. I.; Gorbachev, R. Interfacial Ferroelectricity in Marginally Twisted 2D Semiconductors. *Nat. Nanotechnol.* **2022**, *17*, 390−395.

(11) Rogée, L.; Wang, L.; Zhang, Y.; Cai, S.; Wang, P.; Chhowalla, M.; Ji, W.; Lau, S. P. Ferroelectricity in Untwisted Heterobilayers of Transition Metal Dichalcogenides. *Science* **2022**, *376*, 973−978.

(12) Deb, S.; Cao, W.; Raab, N.; Watanabe, K.; Taniguchi, T.; Goldstein, M.; Kronik, L.; Urbakh, M.; Hod, O.; Ben Shalom, M. Cumulative Polarization in Conductive Interfacial Ferroelectrics. *Nature* **2022**, *612*, 465−469.

(13) Magorrian, S. J.; Enaldiev, V. V.; Zolyomi, V.; Ferreira, F.; Fal'ko, V. I.; Ruiz-Tijerina, D. A. Multifaceted Moire Superlattice Physics in Twisted WSe_2 Bilayers. *Phys. Rev. B* **2021**, *104*, No. 125440.

(14) Enaldiev, V. V.; Ferreira, F.; Fal'ko, V. I. A Scalable Network Model for Electrically Tunable Ferroelectric Domain Structure in Twistronic Bilayers of Two-Dimensional Semiconductors. *Nano Lett.* **2022**, *22*, 1534−1540.

(15) Bennett, D.; Remez, B. On Electrically Tunable Stacking Domains and Ferroelectricity in Moiré Superlattices. *npj 2D Mater. Appl.* **2022**, *6*, No. 7.

(16) Bennett, D. Theory of Polar Domains in Moire Heterostructures. *Phys. Rev. B* **2022**, *105*, No. 235445.

(17) Hod, O. Quantifying the Stacking Registry Matching in Layered Materials. *Isr. J. Chem.* **2010**, *50*, 506−514.

(18) Marom, N.; Bernstein, J.; Garel, J.; Tkatchenko, A.; Joselevich, E.; Kronik, L.; Hod, O. Stacking and Registry Effects in Layered Materials: The Case of Hexagonal Boron Nitride. *Phys. Rev. Lett.* **2010**, *105*, No. 046801.

(19) Blumberg, A.; Keshet, U.; Zaltsman, I.; Hod, O. Interlayer Registry to Determine the Sliding Potential of Layered Metal Dichalcogenides: The Case of 2H-MoS_2. *J. Phys. Chem. Lett.* **2012**, *3*, 1936−1940.

(20) Hod, O. The Registry Index: A Quantitative Measure of Materials Interfacial Commensurability. *ChemPhysChem* **2013**, *14*, 2376−2391.

(21) Leven, I.; Krepel, D.; Shemesh, O.; Hod, O. Robust Superlubricity in Graphene/*h*-BN Heterojunctions. *J. Phys. Chem. Lett.* **2013**, *4*, 115−120.
(22) Leven, I.; Guerra, R.; Vanossi, A.; Tosatti, E.; Hod, O. Multiwalled Nanotube Faceting Unravelled. *Nat. Nanotechnol.* **2016**, *11*, 1082−1086.
(23) Oz, I.; Leven, I.; Itkin, Y.; Buchwalter, A.; Akulov, K.; Hod, O. Nanotube Motion on Layered Materials: A Registry Perspective. *J. Phys. Chem. C* **2016**, *120*, 4466−4470.
(24) Cao, W.; Hod, O.; Urbakh, M. Interlayer Registry Index of Layered Transition Metal Dichalcogenides. *J. Phys. Chem. Lett.* **2022**, *13*, 3353−3359.
(25) Leven, I.; Azuri, I.; Kronik, L.; Hod, O. Inter-Layer Potential for Hexagonal Boron Nitride. *J. Chem. Phys.* **2014**, *140*, No. 104106.
(26) Ouyang, W.; Sofer, R.; Gao, X.; Hermann, J.; Tkatchenko, A.; Kronik, L.; Urbakh, M.; Hod, O. Anisotropic Interlayer Force Field for Transition Metal Dichalcogenides: The Case of Molybdenum Disulfide. *J. Chem. Theory Comput.* **2021**, *17*, 7237−7245.
(27) Yang, Q.; Wu, M.; Li, J. Origin of Two-Dimensional Vertical Ferroelectricity in WTe_2 Bilayer and Multilayer. *J. Phys. Chem. Lett.* **2018**, *9*, 7160−7164.
(28) Henkelman, G.; Uberuaga, B. P.; Jónsson, H. A Climbing Image Nudged Elastic Band Method for Finding Saddle Points and Minimum Energy Paths. *J. Chem. Phys.* **2000**, *113*, 9901−9904.
(29) Enaldiev, V. V.; Ferreira, F.; Magorrian, S. J.; Fal'ko, V. I. Piezoelectric Networks and Ferroelectric Domains in Twistronic Superlattices in WS_2/MoS_2 and $WSe_2/MoSe_2$ Bilayers. *2D Mater.* **2021**, *8*, No. 025030.
(30) Naik, M. H.; Maity, I.; Maiti, P. K.; Jain, M. Kolmogorov−Crespi Potential for Multilayer Transition-Metal Dichalcogenides: Capturing Structural Transformations in Moiré Superlattices. *J. Phys. Chem. C* **2019**, *123*, 9770−9778.
(31) Liao, M.; Nicolini, P.; Du, L.; Yuan, J.; Wang, S.; Yu, H.; Tang, J.; Cheng, P.; Watanabe, K.; Taniguchi, T.; Gu, L.; Claerbout, V. E. P.; Silva, A.; Kramer, D.; Polcar, T.; Yang, R.; Shi, D.; Zhang, G. Uitra-Low Friction and Edge-Pinning Effect in Large-Lattice-Mismatch Van Der Waals Heterostructures. *Nat. Mater.* **2022**, *21*, 47−53.
(32) Kresse, G.; Furthmuller, J. Efficient Iterative Schemes for Ab Initio Total-Energy Calculations Using a Plane-Wave Basis Set. *Phys. Rev. B* **1996**, *54*, 11169−11186.
(33) Giannozzi, P.; Baroni, S.; Bonini, N.; Calandra, M.; Car, R.; Cavazzoni, C.; Ceresoli, D.; Chiarotti, G. L.; Cococcioni, M.; Dabo, I.; Dal Corso, A.; de Gironcoli, S.; Fabris, S.; Fratesi, G.; Gebauer, R.; Gerstmann, U.; Gougoussis, C.; Kokalj, A.; Lazzeri, M.; Martin-Samos, L.; Marzari, N.; Mauri, F.; Mazzarello, R.; Paolini, S.; Pasquarello, A.; Paulatto, L.; Sbraccia, C.; Scandolo, S.; Sclauzero, G.; Seitsonen, A. P.; Smogunov, A.; Umari, P.; Wentzcovitch, R. M. Quantum Espresso: A Modular and Open-Source Software Project for Quantum Simulations of Materials. *J. Phys.: Condens. Matter* **2009**, *21*, No. 395502.
(34) Perdew, J. P.; Burke, K.; Ernzerhof, M. Generalized Gradient Approximation Made Simple. *Phys. Rev. Lett.* **1996**, *77*, 3865−3868.
(35) Grimme, S.; Antony, J.; Ehrlich, S.; Krieg, H.; Consistent, A. and Accurate Ab Initio Parametrization of Density Functional Dispersion Correction (DFT-D) for the 94 Elements H-Pu. *J. Chem. Phys.* **2010**, *132*, No. 154104.
(36) Grimme, S.; Ehrlich, S.; Goerigk, L. Effect of the Damping Function in Dispersion Corrected Density Functional Theory. *J. Comput. Chem.* **2011**, *32*, 1456−1465.
(37) Monkhorst, H. J.; Pack, J. D. Special Points for Brillouin-Zone Integrations. *Phys. Rev. B* **1976**, *13*, 5188−5192.

https://doi.org/10.1021/acsami.2c20411
ACS Appl. Mater. Interfaces 2022, 14, 57492−57499